Preprint submitted to J. Chem. Phys. (2005)

EFFECT OF NANO–CONFINEMENT ON LIQUID CRYSTAL POLYMER CHAINS.

Davide Micheletti, Luca Muccioli, Roberto Berardi,

Matteo Ricci, and Claudio Zannoni,

Dipartimento di Chimica Fisica e Inorganica and INSTM,
Università di Bologna,
Viale Risorgimento 4, 40136 Bologna, Italy.

August 2005

Abstract

We apply a Monte Carlo polymerization model for Gay-Berne monomers that we have recently introduced [J. Chem. Phys. 121, 9123 (2004)] to investigate with computer simulations the effects of nanoconfinement and anchoring type on the structure of the main chain liquid-crystal polymers formed in thin films, in the presence of several types of surface alignment: parallel to the interface (random and uniform) or perpendicular to it (homeotropic). We perform first a study of the confined monomers and then we examine the features of the polymer chains obtained from an isotropic or nematic sample. We find a significant effect of the anchoring conditions on the characteristics of the chains and particularly striking differences between planar and homeotropic boundaries. Furthermore, our results indicate that the choice of different anchorings could be used to tune the linearity and degree of polymerization of the chains.

1 Introduction

Thin films of nematic liquid crystals (LC) play a very important role in technological applications.[1] First and foremost is their use in displays and electrooptical devices,[2,3] but more recently a number of other applications, particularly as biosensors,[4] smart elastomeric materials[5] and nanoscale devices[6,7] are emerging. Many of these applications rely on the fact that, close to the film boundaries, the ordering of the LC is affected by the physical or chemical inhomogeneities of the surfaces, with the nematic acting as an amplifier of these interfacial perturbations[4] creating various types of local molecular organizations.[8] The influence of surface effects on the nematic properties propagates to distances up to tens of micron,[4] but it becomes even more interesting when the LC phase thickness reduces to a few molecular layers,[9,10] giving raise to molecular organizations with novel properties with respect to the bulk case. This could also be the case of nano–thin film separating two micron size colloidal particles where the much larger diameter gives an effectively flat interface.[11] Apart from the technological interest, the influence of confinement on the phase behavior of LC is of high fundamental interest, and has been widely studied in a variety of environments ranging from simple suspended thin films to micrometric pores and nano–sized systems.[12] In particular, the confinement is found to induce capillary condensation of a nematic due to the aligning action of the confining surface on an otherwise massive isotropic fluid. In that case, the short range liquid crystal-wall interaction creates a weak nematic ordering, which decays into the isotropic bulk. Various surface treatments have been developed, particularly in display technology, to induce and control some specifically tailored organizations of LC materials. For instance, alignment perpendicular to the surface (homeotropic) can be obtained by coating, e.g. with lecithin[9] or certain polyimides,[13–15] while alignment in the cell plane can be obtained by mechanically rubbing a polymer deposited film,[16–19] with SiO_2 sublimation,[20,21] or with suit-

able gold deposition.[4] On the other hand, untreated hydrophilic mica or a flat gold layer cause a "planar parallel" orientation[9] of the director of nematic LC.[9] In non-display applications an increasingly important technique for consolidating the specific LC molecular organizations obtained is that of polymerizing suitably chosen prepolymer-monomer LC mixtures.[22] This strategy for controlling surface interactions offers in principle the possibility of creating thin films of polymer with well defined molecular organization and optical or mechanical properties.[7,23]

Until now, there have been various theoretical studies of low molar mass LCs in restricted geometries with the help of Monte Carlo (MC) coarse-grained[10,24–31] and lattice simulations[32,33] but many aspects still remain to be clarified, in particular those linked to specific surface orienting effects rather than just confinement.

Regarding the properties of confined polymer solutions and polymer thin films,[34] they have been the subject of extensive studies due to the interest in many applications such as lubrication, colloidal dispersion, and chromatographic separations. The properties of the confined solutions depend on many factors such as the nature of the confining surface, the geometry of the confining object, and chain flexibility. Therefore, despite a large number of computer simulations that have been reported in literature,[35–47] there is still a keen interest in understanding the behavior and properties of such systems. For instance, very little is available on the effects of various boundary conditions on phase organization of prepolymers and on the resulting polymer chain organization after the reaction has taken place.

In this paper we are interested in modelling the effect of confinement and polymerization on the structure of MC-LCP[48] grown in a nano–confined environment, by using a recently proposed coarse grained polymerization model for Gay-Berne (GB) monomers.[49] We shall also investigate the effects of walls confinement at nanometric scale on the ordering of monomers, focusing on five different surface anchorings: homeotropic weak (HOw), homeotropic strong (HOs), random planar (RP), uniform alignment (UA), and purely repulsive confining walls (RW).

2 Model

The systems under study are constituted by a liquid phase of either LC monomers or oligomers, confined between two parallel smooth surfaces at nanometric separation, whose properties are governed by molecule–molecule and molecule–surface interactions. The transformation between the monomeric and the polymeric phase is accomplished by a series of irreversible reactions steps, which allow the formation of bonds between the growing chain and unreacted monomer particles.

The total energy per particle of the system consists of both non–bonded and bonded intra–chain terms. Normalizing to the number N of initial monomers in the sample, we can write the total dimensionless energy per particle U^* as

$$U^* \;=\; U/\epsilon_0 \;=\; U^*_{GB} \;+\; U^*_{bond} + \; U^*_w, \tag{1}$$

where U^*_{GB} and U^*_{bond} are the monomer–monomer non–bonded and bonded interactions and U^*_w is the wall–monomer interaction, and ϵ_0 is an unit for the energy scale to be introduced later.

We describe the interaction between monomeric liquid crystalline units with an attractive–repulsive Gay–Berne pair potential[50] that has been shown to yield smectic and nematic LC phases (for a review see[51]). The total non–bonded interaction term U_{GB} is calculated over all pairs as

$$U^*_{GB} = \frac{1}{N}\sum_{i<j}(1-b_{ij})U^*_{GB}(\hat{\mathbf{u}}_i, \hat{\mathbf{u}}_j, \mathbf{r}_{ij}), \tag{2}$$

with $\sum_{i<j} = \sum_{i=1}^{N-1}\sum_{j=i+1}^{N}$, and $b_{ij} = 1$ if i and j are bonded and zero otherwise. The GB interaction energy between two particles i, j consists of an anisotropic and shifted form of the 12-6 LJ potential:[50,52]

$$\begin{aligned} U^*_{GB}(\hat{\mathbf{u}}_i,\hat{\mathbf{u}}_j,\mathbf{r}_{ij}) &= 4\epsilon^{(\mu,\nu)}(\hat{\mathbf{u}}_i,\hat{\mathbf{u}}_j,\hat{\mathbf{r}}_{ij}) \\ &\times\left\{\left[\frac{\sigma_s}{r_{ij}-\sigma(\hat{\mathbf{u}}_i,\hat{\mathbf{u}}_j,\hat{\mathbf{r}}_{ij})+\sigma_s}\right]^{12} - \left[\frac{\sigma_s}{r_{ij}-\sigma(\hat{\mathbf{u}}_i,\hat{\mathbf{u}}_j,\hat{\mathbf{r}}_{ij})+\sigma_s}\right]^{6}\right\}. \end{aligned} \tag{3}$$

The analytical expressions for the interaction strength function $\epsilon(\hat{\mathbf{u}}_i, \hat{\mathbf{u}}_j, \hat{\mathbf{r}}_{ij})$ and for the range function $\sigma(\hat{\mathbf{u}}_i, \hat{\mathbf{u}}_j, \hat{\mathbf{r}}_{ij})$, as well as the specific parameters used here, are the same introduced in references.[50,51]

Regarding the modelling of the bonded interactions, every molecule carries either one or two reaction sites (which allow it to act respectively as a radical initiator or as a monomer) that can become links upon reaction. In that case the GB interaction between a linked pair of monomers is replaced by a sum of stretching and bending Finitely Extendable Nonlinear Elastic Potential[53] (FENE) contributions, so that the bonded energy per particle term is

$$U^*_{bond} = \frac{1}{N} \sum_{i<j} b_{ij} [U^*_s(s_{ij}) + U^*_\theta(\theta_{ij}) + U^*_0], \tag{4}$$

where s_{ij} and θ_{ij} are the bond length and bending angle. The FENE pair interaction stretching $U^*_s(s_{ij})$ and angular $U^*_\theta(\theta_{ij})$ energies between two reaction sites i, j can be written in general terms as[53,54]

$$U^*_\xi(\xi_{ij}) = -K_\xi \ln \left[1 - \left(\frac{\xi_{ij} - \xi_{eq}}{Q_\xi - \xi_{eq}} \right)^2 \right], \tag{5}$$

where $\xi_{ij} = s_{ij}$ for the stretching, and $\xi_{ij} = \theta_{ij}$ for the bending energy. Here ξ_{eq} is either the equilibrium bond length s_{eq} or bend angle θ_{eq}, and $K_\xi = \kappa_\xi (Q_\xi - \xi_{eq})^2/2$, where κ_ξ is a stiffness parameter, and $|Q_\xi - \xi_{eq}|$ is the maximum displacement from the equilibrium value. If the distance or the angle are equal to s_{eq} or θ_{eq} respectively, then the pair bonding energy is equal to the U^*_0 value.

2.1 Surface–monomer interaction

The specific anisotropic surface–monomer interaction has been taken into account by embedding two spherical sites, labelled A and B, within each GB ellipsoid (see Figure 1). The interaction energy between the sites of particle i and the smooth wall, $U^*_w(i)$, is given by a shifted (n, m) potential

$$U^*_w(i) = f(\hat{\mathbf{u}}_i)\ K_w \sum_{site=A,B} \left[\left(\frac{\sigma_w}{r_{wi}^{site} + \sigma_w} \right)^n - \alpha_i^{site} \left(\frac{\sigma_w}{r_{wi}^{site} + \sigma_w} \right)^m \right], \tag{6}$$

where K_w is the interaction strength term, $f(\hat{\mathbf{u}}_i)$ is an anisotropic angular term which influences particles alignment with respect to an in-plane surface axis, α_i^A and α_i^B are site specific coefficients, and ${r_w}_i^A$ and ${r_w}_i^B$ are the sites distances from the wall (see Fig. 1). The σ_w parameter has been chosen equal to σ_s, i.e. the short axis of a GB monomer. As for the choice of the exponents, we recall that by integrating the dispersion interaction between a LJ particle and an infinite slab formed by LJ centres, an overall particle–surface potential governed by a $(9,3)$ law is obtained. In the literature, the particle–surface energy is usually modelled with a variety of repulsive and attractive exponents, like the $(10,4)$ exponents implemented by Steuer *et al.*,[26] and the $(9,3)$ used by Caprion *et al.*[27] Considering that most common materials mentioned in the Introduction are far from being completely smooth[9,20,21] and also the existence of electrostatic interactions[13–19] between surfaces and molecules, we have arbitrarily set the repulsive coefficient n to a softer value of 6 to allow for some surface penetration, while keeping $m = 3$. In Table 1 we list the coefficients used to parametrize the various anchoring presented in the introduction.

In the RW case with $f(\hat{\mathbf{u}}_i) = 1$, $\alpha_i^A = 1$, and $\alpha_i^B = 1$, there is no preferential orientation for molecules at the surface and the surface interactions cutoff is equal to 1, in order to have a purely repulsive confinement.

The RP parameterization is the same as RW, except for the the surface interaction cutoff, which has been set to the distance between the two surfaces L_x: this choice has also been adopted for all other anchoring models.

By setting $f(\hat{\mathbf{u}}_i) = (\hat{\mathbf{u}}_i \cdot \hat{\mathbf{n}})^2$, $\alpha_i^A = 1$, and $\alpha_i^B = 1$ we favor instead an uniform alignment anchoring (UA) to the surface along the $\hat{\mathbf{n}} \equiv z$ direction of the laboratory frame.

Homeotropic anchoring is finally obtained choosing $f(\hat{\mathbf{u}}_i) = 1$, and $\alpha_i^B = 0$. In this case the B site does not interact with the surface and the combination of a preferential interaction of only one of the molecular ends and a close surface

packing tends to align particles perpendicularly. This parameterization specializes in strong (HOs) and weak (HOw) homeotropic anchoring, when we further specify $\alpha_i^A = 2$ or 1.

The particle–wall interaction strength value has been set to $K_w = 9$ in order to have the maximum wall–site U_w^* energy equal to the strongest U_{GB}^* side–by–side interaction. In the case of homeotropic anchoring instead, we have counterbalanced the lacking B site interaction with a stronger constant $K_w = 18$ for HOw, and $K_w = 36$ for HOs. This latter parameterization results in a maximum interaction twice the U_{GB}^* side–by–side energy.[51,52] In other words, the HOs parameterization ensures "strong anchoring" conditions, i.e. that the surface–LC interaction is stronger than the interaction between the first LC layer and the LC bulk.

3 Confined monomer simulations

As a preliminary stage we have studied the ordering of the confined monomeric system in presence of the five anchoring of Tab. 1. These simulations have also provided the starting configurations for the nano–confined polymerization described in the next section.

We have simulated, using the MC technique under canonical constant (NVT) conditions, systems of $N = 4096$ GB monomeric particles contained in a cubic box with periodic boundaries[55,56] along the y and z axes and confined between two planar slabs along the x direction. The sample dimensions employed were $L_x = L_y = L_z = 24\sigma_0$, which correspond to a scaled number density $\rho^* = N\sigma_0^3/V = 0.3$. The parameterization chosen for the GB interactions is that of ref.[52] with $\mu = 1$, $\nu = 3$, short axis $\sigma_s = 1\ \sigma_0$, long axis $\sigma_e = 3\ \sigma_0$, and well depths $\epsilon_s = 1\ \epsilon_0$, $\epsilon_e = 0.2\ \epsilon_0$, giving isotropic, nematic and smectic phases. In particular, the bulk phase of this system presents a nematic–isotropic phase transition at scaled temperature $T_{NI}^* \approx 3.55$.[52] The parameters σ_0 and ϵ_0 are the units of length and energy: if

one GB ellipsoid is considered as a typical calamitic mesogen with $T_{NI} \approx 355$ K, they can be estimated as $\sigma_0 \approx 5$Å and $\epsilon_0 = k_B T_{NI}/T^*_{NI} \approx 1$ kcal/mol. With this parameterization, the thickness of the confined sample (which is six particles lengths) is approximately 12 nm.

For every confinement case we have performed a sequence of cooling MC runs starting from an equilibrated isotropic sample at $T^* = 3.8$, while higher temperature samples have been obtained by heating. For every state point we have performed equilibrations at least 200 MC kcycles long (1 cycle being equal to N attempted MC moves), followed by a production run of the same length.

We have characterised these systems by considering the temperature dependence of the average total energy $\langle U^* \rangle$, and the second rank orientational order parameter $\langle P_2^{(d)} \rangle$, calculated with respect to the LC phase director $\hat{\mathbf{d}}$,[57] and compared them with the bulk GB system of ref.[52]

For low enough temperatures we have observed the occurence of isotropic-nematic and nematic-smectic phase transitions, which appeared in all cases the temperature range $T^* = 3.4 - 3.5$, and $2.0 - 2.2$ respectively. In this paper we focus on the properties of the nematic phase and Figure 2 shows the average order parameter $\langle P_2^{(d)} \rangle$ as a function of T^*, and how the various boundary conditions affect the nematic-isotropic transition temperature (T^*_{NI}).

Starting with the RW confinement, we see that it produces the larger lower temperature shift for NI transition when compared with the results for the bulk phase. This result can be ascribed to the combination of two phenomena, whose separate contributions are hard to disentangle: the replacement of a part of the bulk intermolecular energy with the particle-walls interactions with no surface anisotropic alignment, and the slight variation of sample density given by the repulsive softness of the walls. While for containers at least of micrometric scale, the sample volume can be considered constant and walls softness can be neglected, when going to the nanometric scale the effective volume availaible to the molecules between

soft surfaces is not a geometrical quantity and has to be measured, and furthermore it depends on temperature. For our samples we have estimated as a lower bound of the effective density $\rho^* = 0.285$; this 5% density variation is sufficient to change noticeably the phase GB diagram and the direct comparison with the bulk results for $\rho^* = 0.3$ is more difficult. Nonetheless, all anchoring potentials studied share the same repulsive term and consequently can be consistently compared with the RW results, which we choose as reference confined system; moving back to the $\langle P_2^{(d)} \rangle$ plot of Fig. 2, we can observe a relatively sharp NI transition for the bulk, RW, and RP cases. The HOw case shows instead a much weaker transition temperature, and gives samples with a partial residual orientational ordering immediately above T^*_{NI} (paranematic). The UA and HOs anchorings produce an almost continuous $\langle P_2^{(d)} \rangle$ transition and show a net residual order also at the highest temperature studied. The strong orienting effect of the boundaries is not uniform across the sample and produces well defined and ordered molecular layers near to the confining surfaces (see sample snapshots in Fig. 3).

In Fig. 2 we also report the average $\langle U^* \rangle$ values as a function of T^* and we observe again how the RW and RP internal energy curves are similar in shape to the bulk case but shifted in temperature. Furthermore, the $\langle U^* \rangle$ at the NI transition for the RP sample is close to that for the RW anchoring: the isotropic attractive surface–monomer interaction does not affect significantly the NI transition. For the HOs, and UA boundaries the energy profiles show only modest changes in slope around T^*_{NI}, confirming again that the nano–confinement promotes NI transition of a second order character.

We have estimated the T_{NI} from the temperature derivative of the average energy, order parameter, and the second and third cumulants of their energy distributions, as described in ref.[58] The cumulants showed evidence of a weak first order phase transition for the RW ($T^*_{NI} = 3.30$), RP ($T^*_{NI} = 3.30$), and HOw ($T^*_{NI} = 3.40$) anchorings, while for HOs and UA confinement the nematic–isotropic transition

appears to be of second–order type ($T^*_{NI} \approx 3.40$). We also have estimated the adimensional variation in energy and entropy at the transition ΔU^*_{NI} and ΔS^*_{NI}, by linearly fitting the two $\langle U^* \rangle$ branches above and below T^*_{NI}, while excluding the transition region itself. The values of these functions at T^*_{NI} give respectively U^*_N and U^*_I of the two phases at equilibrium. Since $\Delta A^*_{NI} = 0$ it is possible to estimate $\Delta S^*_{NI} = \Delta U^*_{NI}/T^*_{NI}$, and we have found $\Delta S^*_{NI} = 0.53$ for the bulk sample, while RW and RP confinement conditions give ΔS^*_{NI} values similar but slightly lower than that of the bulk sample (0.48 for RW, 0.52 for RP), and only for the HOw sample the lower change in entropy at the transition $\Delta S^*_{NI} = 0.42$ is reminiscent of the residual order above T^*_{NI}. We can rationalize these data in terms of the nano–confined isotropic phase being somewhat more ordered and with lower entropy than the bulk case because of the break in symmetry due to the surface.

Finally, in Fig. 3 we show a selection of equilibrated sample snaphots, colour coded to indicate the monomer orientation with respect to the laboratory z axis direction: for orientations between 0° and 90°, the colour gradually changes from yellow (parallel) to blue (perpendicular) as shown in the palette. These snapshots show the origin of the so-called "surface memory effect":[59,60] by heating the sample from $T^* = 2.8$ to $T^* = 3.8$ the orientational and positional order of the monomers near the walls does not disappear, and the original aligned state condition can be recovered cooling again the paranematic sample.

4 Confined polymerization simulation

4.1 Sample preparation

To study the polymerization process, we have considered two larger systems of $N = 16384$ monomeric GB particles at temperatures: $T^* = 2.8$ and 3.8, corresponding to a nematic and an isotropic phase for the RP, UA, and HOs anchorings (cfr. Figure 2). The RW anchoring has not been taken into account because we are

interested in studying the effect of attractive surface interactions. Also, the HOw anchoring will not be discussed here since we have found results to be similar at a smaller scale to the HOs case.

The polymerization reaction cell was an orthorhombic sample with periodic boundaries along y and z directions, and whose dimensions were $L_y = L_z = 48\sigma_0 \approx 24$ nm, corresponding to a distance between the two planar confining walls $L_x = 24\sigma_0 \approx 12$ nm as for the monomeric systems. To build up these enlarged samples we have used the following procedure: for every surface anchoring case we have equilibrated a cubic $N = 4096$ monomeric sample for 100 MC-NVT kcycles in presence of a weak external field producing a coupling energy lower than 1% of the GB interactions, that introduce a bias for the director orientation along the z laboratory axis, without significantly changing the order (see Fig. 3). Then, we have assembled four periodic replicas along the y and z directions, switched the field off, and performed a 150 MC kcycles equilibration of the enlarged samples. The chain polymerization reactions have then been followed for 100 MC-NVT kcycles, adopting for the non–bonding interactions the same parameter set used for the confined monomers, and for the bonded potential the parameters reported in Ref.[49] The number of radical initiators has been set to $N_r = 150$, corresponding to a mole fraction $N_r/N = 9.2 \times 10^{-3}$. We have not considered here a mechanism of chain transfer, so the total number of chains N_c coincides with N_r and remains constant all over the MC simulation. After the chain growth MC run, the samples have been left to relax for further $M = 200$ MC kcycles.

4.2 Single chain properties

In Fig. 4 we show a three-dimensional view of the polymer snapshots for the various anchoring types at the end of the relaxation run (we use the same colour coding). We see at once that chains have developed for all anchorings but with different morphology. These nano–confined polymeric chains have been analysed

by focusing on four features: length, shape, structure, and orientational order. To ease the comparison, we have also considered a bulk sample with $N = 4096$ monomers, and we have performed a simulation with the same mole fraction of radical initiators.

We show first, in Table 2, the monomer conversion $C_{mon} = N_{pol}/N$ computed at the end of the simulated polymerization, which is an indicator of the effectiveness of the chain growth reaction. In the previous expression $N_{pol} = \sum_x xN(x)$ is the number of reacted monomers, while the length density $N(x)$ counts the number of macromolecules formed by x monomeric units, where $N_c = \sum_x N(x)$ is the total number of chains. The polymer length distributions have been further characterized by computing the standard indeces, i.e. the ratios of the moments of the chains length distribution, number–average degree of polymerization

$$\bar{x}_n = N_{pol}/N_c, \tag{7}$$

weight–average degree of polymerization

$$\bar{x}_w = \frac{1}{N_{pol}} \sum_x x^2 N(x), \tag{8}$$

and polydispersity

$$\bar{I}_d = \bar{x}_w/\bar{x}_n. \tag{9}$$

In the confined systems the conversion C_{mon} ranges between 5% and 15% for HOs, while it is around 50% for all other anchoring types both at low and high temperature. Thus, in all samples the polymeric chains form a non fully connected network enclosing large amounts of unreacted monomers. This has also been observed for chains grown in the bulk phase[49] with the difference that, as shall we see later, the confinement can induce a spatial non-uniformity in the resulting structures. For the nematic samples with UA and RP anchorings, the chains grow parallel to the walls along the phase director (see Fig. 4), and consequently there are no geometrical constraints to the radical propagation. The polymerization degree $\bar{x}_n$

increases as temperature decreases while order increases, and all indeces are similar to the bulk values, only with a tendency for the UA sample to give slightly higher values. This behavior is consistent with a higher probability of successful MC reactive moves in the low–temperature systems, where the synergic effects of confinement and orientational order favors the polymerization. In the nematic with homeotropic confinement instead, radicals close to the surfaces have reduced positional and orientational mobilities due to the strong anisotropic aligning potential, and chains grow preferentially straight and perpendicular to the walls (see Fig. 4). In this case, the average degree of polymerization $\bar{x}_n$ has an upper bound imposed by the ratio between walls separation and monomer length, which is $L_x/\sigma_e \approx 6$, and the resulting conversion is only few units percent (see Table 2).

In the isotropic samples the additional effect on properties due to the confinement with respect to the bulk polymer is not very relevant for the UA case. For the RP boundaries instead, $\bar{x}_n$ and $\bar{x}_w$ are smaller than in the bulk, hinting to a surface effect which partially unfavors the chain growth. The $\bar{I}_d$ index is not influenced in both RP and UA cases. For the HOs sample the presence of an isotropic fluid in the sample center weakens the geometrical constrains on the maximum attainable conversion measured for the nematic sample and C_{mon} triplicates while $\bar{I}_d$ slightly increases. Notice that, since the radicals initiators have been created at random positions, and since the homeotropic confinement invariably terminates the growth of every chain whose propagating radical reaches a surface, the HOs confinement determines a higher value of $\bar{I}_d$ with respect to the UA and RP cases, that are characterized by a narrow distribution of chain lengths. These simulation results suggest the appealing possibility of dimensioning a nano–confined nematic reaction cell with HOs anchoring to taylor a desired maximum degree of polymerization.

We have also calculated (and reported in Table 3) other specific chain length

observables as the average square end–to–end distance defined as

$$\langle r_{ee}^2 \rangle = \frac{1}{MN_c} \sum_{m=1}^{M} \sum_{k=1}^{N_c} r_{e,e}^{(m,k)^2}, \tag{10}$$

where $r_{ee}^{(m,k)}$ is the distance between the terminal tips of the first and last monomeric units for the k–th chain in the m–th MC configuration, and the average square gyration radius

$$\langle r_{gyr}^2 \rangle = \frac{1}{MN_c} \sum_{m=1}^{M} \sum_{k=1}^{N_c} \frac{1}{x_k} \sum_{i=1}^{x_k} r_{i,cm}^{(m,k)^2}, \tag{11}$$

where $r_{i,cm}^{(m,k)}$ is the distance between the i–th monomer position and the center of mass for the k–th chain of the m–th configuration. During the MC relaxation run, these distances have showed only small variations (of the order of 1%) from the values attained at the end of the chain growth run. This behavior suggests that after the polymerization reaction is stopped, in spite of being the conversions not higher than 60%, the decrease of diffusion coefficient and the entangling of chains allows only for small fluctuations of the properties over the sampling length explored by our MC simulations; this is in line with the mean square displacements observed.

If we consider the contour length $r_{max}^* = s_{eq}(\bar{x}_n - 1) + \sigma_e \bar{x}_n$, which gives the limiting average length of a perfectly straight chain, and compute the ratios $l_{ee} = \langle r_{ee}^{*\,2} \rangle^{1/2} / r_{max}^*$ for all cases of confinement and temperature, we see that those calculated for the bulk sample are very similar to those relative to the RP boundary at both scaled temperatures $T^* = 2.8$, and 3.8, and this is also the case for the UA at $T^* = 2.8$. Instead, for the UA and HOs confinements at $T^* = 3.8$ there is an increase of l_{ee} of about 40% with respect to the bulk, due to the aligning effect of the anchoring on polymer chains near to the surfaces (see snapshots in Fig. 4). The similarities of these l_{ee} ratios with the bulk value at $T^* = 2.8$ indicate that in presence of an ordered phase the anchoring induced alignment does not further influence this chains property. On the contrary, in the $T^* = 3.8$ isotropic phase the chain spatial configuration is strongly affected by the surface interaction as we

observe for UA and HOs anchorings, where the yellow and blue colours of aligned chains fade respectively to blue and red when moving to the center of the box (see snapshots in the right column of Fig. 4), while for the RP anchoring, we have not observed any significative change in chains orientation at the surface with respect to the center of the box (see top-right snapshot of Fig. 4). The same comment applies to the ratio $\langle {r^*_{ee}}^2 \rangle / \langle {r^*_{gyr}}^2 \rangle$ in Table 3, which also provides information on the linearity of chains. It is worth noticing though, that in the isotropic phase of the UA and HOs samples, the ratio $\langle {r^*_{ee}}^2 \rangle / \langle {r^*_{gyr}}^2 \rangle$ is higher than the theoretical value of 6 predicted for a model of freely jointed (gaussian) chains,[61] which is observed instead for the RP and bulk cases.

4.3 Polymer organization in the slab

To further characterize the structures and anisotropy of the confined chains, we have calculated the density distribution $g_w(x^*)$, giving the probability of finding a polymer repeating unit (or a monomer, for the bulk case) at a distance x^* from the nearest wall surface ($x^* = 0$, and $x^* = 24$) towards the simulation box center:

$$g_w(x^*) = \frac{\sigma_0^2}{L_z L_y \rho^* C_{mon}} \langle \delta(x^* - x_i^*) \rangle_i, \tag{12}$$

where the ensemble average $\langle ... \rangle_i$ is performed over the particles of all MC configurations (sampled with a stride of 20) of the relaxation run. To allow the comparison between the various confinement systems the resulting histograms have been normalised to the monomer conversion C_{mon}. We have also studied the spatial distribution of orientational order near the boundary walls, and considered the alignment of polymer repeating units with respect to the z axis of the reference frame, computing the average order parameter profile $\langle P_2^{(z)}(x^*) \rangle = \langle (\frac{3}{2}(\mathbf{u}_i \cdot \mathbf{z}) - \frac{1}{2}) \delta(x^* - x_i^*) \rangle_i$ as a function of the distance x^* of a repeating unit from the nearest surface. In Fig. 5 we have plotted both $g_w(x^*)$ and $\langle P_2^{(z)}(x^*) \rangle$ curves for the isotropic ($T^* = 3.8$), and nematic ($T^* = 2.8$) polymeric samples.

In the RP case, at $T^* = 2.8$, the order $\langle P_2^{(z)}(x^*)\rangle$ maintains approximately the same value ≈ 0.8 independently of the distance from the walls. At $T^* = 3.8$ instead, the confinement induces a residual orientational order only for the repeating units in contact with the surfaces ($\langle P_2^{(z)}(x^*)\rangle \approx 0.2$ at $x^* \leq 1$), and none for distances $x^* > 1$. The $g_w(x^*)$ profiles for the RP systems show the presence of structured layers of repeating units parallel to the walls (see also Fig. 4), as far as $x^* \leq 4$ at $T^* = 2.8$, and $x^* \leq 2$ at $T^* = 3.8$. Due to the softness of the surfaces, the first layer of repeating units is partially embedded (for approximately half width σ_s) in the confining wall, so that the maximum of $g_w(x^*)$ is at $x^* \approx 0$, while the successive maxima are spaced at distances which are roughly multiples of σ_s.

For the UA samples, we observe that the orientational order near the confining surfaces is higher than at the box center ($x^* = 12$), both in the nematic, and in the isotropic phase. In this later case, $\langle P_2^{(z)}(x^*)\rangle$ decreases smoothly moving away from the surfaces, and reaches an isotropic zero value at $x^* \approx 6$, while for the former temperature it reaches a plateau value corresponding to the bulk phase order parameter. If we consider both UA temperatures, the positional structure disappears for $x^* > 4$ (see also Fig. 4). Surprisingly, the effect of UA boundaries produces sharper $g_w(x^*)$ density profiles in the isotropic than in nematic phase, especially around $x^* \approx 0$, while at larger distances ($x^* > 8$), we observe in the isotropic phase a density decrease with respect to the nematic one. This behavior can be explained in terms of higher reaction probability in ordered fluid phases: near the UA surfaces the high orientational ordering ($\langle P_2^{(z)}(x^*)\rangle \simeq 0.9$ for $x^* < 2$, see Fig. 5) strongly favors the polymerization processes near the surface rather than at the center of the box, where due to the low order, we register a smaller monomer conversion. This results also in the observed chain density decrease and a higher fraction of unreacted monomers. On the other hand, at $T^* = 2.8$, due to the uniform orientational order, we have a similar probability of radicals propagation for all surface-monomer separation distances x^*, and consequently, a more uniform

distribution of polymer chains.

In the HOs samples the anchoring induces the macromolecules to align along the x axis, and at $T^* = 2.8$ we observe five homeotropic layers of repeating units (with minima of $\langle P_2^{(z)}(x^*)\rangle \simeq -0.4$, see also Fig. 4), with smectic-like ordering induced by the presence of bonds. In contrast with the confined monomeric sample (see Fig. 3), where the effect is absent, and there is no propagation to the bulk of the surface ordering effect. On the other hand, if we consider the polymeric sample at $T^* = 3.8$ only three layers can be detected, and the chains orientational and positional order in the box center is negligible. In the boundary region at $T^* = 2.8$ only few repeating units with $x^* < 1$ have been observed, and since the very close molecules cannot retain an homeotropic alignment, these particles exhibit a positive order parameter ($\langle P_2^{(z)}(x^*)\rangle \simeq 0.35$) with large error bars. At higher temperature $T^* = 3.8$ we do not observe this behavior, and $\langle P_2^{(z)}(x^*)\rangle \simeq 0$ for $x^* > 1$. The HOs anchoring also determines remarkable differences in the $g_w(x^*)$ profiles: at $T^* = 2.8$, due to linear chains that transverse the sample from one surface to another, we observe well defined maxima over the entire range of x^*. In the isotropic phase these features are smeared out for $x^* > 4$, since the chains waggle around rather than adopting a linear conformation.

To conclude, the aligning effect of HOs and UA anchorings, allow us to control the chain structure and although we cannot prove it directly from our MC simulation, this suggests the possibility of lowering the melt viscosity in the nano–confined sample with respect to the bulk case.

5 Conclusions

In this paper we have presented Monte Carlo simulation results for a nano–confined fluid of Gay Berne liquid crystal monomers and of main–chain liquid crystal polymers.

The confinement was enforced by restricting a LC film between two infinite flat walls, while the monomer or the polymer–surface interactions have been modelled by using a 6–3 attractive–repulsive potential. This choice of a repulsive soft term determines a small temperature variation of the accessible sample volume but does not significantly affect the phenomenological properties.

For the preliminar study of confined GB monomers we have found for our boundaries conditions results similar to those of other low mass confined systems.[10,24–31] We have observed the presence of a residual orientational order in the isotropic phase and a second order nematic–isotropic (strictly paranematic) transition for uniform alignment (UA) and homeotropic strong (HOs) anchorings. We find that LC monomers close to the surfaces are endowed of orientational and positional order both in the nematic and the isotropic phase, hinting at the origin of the so–called "surface memory effect".[59,60]

Concerning the MC-LCP samples, we have found that starting polymerization in the disordered phase, the various surface anchorings strongly and characteristically affect chain structures. In the random planar (RP) boundary there are no evidences of residual orientational order, and this has been confirmed by computing the scaled end–to–end distances $l_{ee} = \langle {r^*_{ee}}^2 \rangle^{1/2} / r^*_{max}$ and gyration radii $\langle {r^*_{ee}}^2 \rangle / \langle {r^*_{gyr}}^2 \rangle$ which do not crucially differ from those calculated for the bulk sample.

Differently, UA and HOs nano–confinement induce an orientational ordering of the chains at the surfaces, and we observe elongated chains with an increase of l^*_{ee} ratio of about 40%, and the highest $\langle {r^*_{ee}}^2 \rangle / \langle {r^*_{gyr}}^2 \rangle$ ratio.

On the other hand, in presence of a nematic (ordered) phase the simulated polymerization process is not considerably influenced by the confinement and this results in the formation of linear chains for all kind of planar boundaries. In the case of HOs anchoring, the growth of chains, whose length roughly corresponds to the distance between the two confining walls has been observed.

The result suggest that it could be possible to tune a LC polymer chain length by choosing reaction cells with homeotropic nano–confined geometries (channels) of selected thickness. In view of the interest for nano–confined polymeric films we believe these findings will stimulate experimental investigations and possibly help in the preparation of materials based on tuning the film anchoring conditions.

Acknowledgement

We thank University of Bologna, and EU (IP NAIMO *Nanoscale Integrated processing of self-organizing Multifunctional Organic Materials*, project reference NMP4-CT-2004-500355, and TMR FULCE *Functional Liquid Crystalline Elastomers*, contract HPRN-CT-2002-00169) for financial support. D.M. thanks Prof. D. Frenkel and SARA Computing Center (Amsterdam) for hospitality during a EU-HPC Europa supported visit.

References

[1] B. Bahadur, editor, *Liquid Crystal applications and uses* (Word Scientific, Singapore, 1989).

[2] M. Schadt, Ann. Rev. Mater. Sci. **27**, 305 (1997), and references therein.

[3] D. Pauluth and K. Tarumi, J. Mater. Chem. **14**, 1219 (2004).

[4] V. K. Gupta, J. J. Skaife, T. B. Dubrovsky and N. L. Abbott, Science **279**, 2077 (1998).

[5] Y. L. Yu, M. Nakano and T. Ikeda, Nature **425**, 145 (2003).

[6] I. W. Hamley, Angew. Chem.-Int. Edit. **42**, 1692 (2003).

[7] M. O'Neill and S. M. Kelly, Adv. Mater. **15**, 1135 (2003).

[8] V. K. Gupta and N. L. Abbott, Science **276**, 1533 (1997).

[9] M. Ruths, S. Steinberg and J. N. Israelachvili, Langmuir **12**, 6637 (1996).

[10] X. Yang and J. Ding, J. Chem. Phys. **121**, 7449 (2004).

[11] J. N. Israelachvili, *Intermolecular and Surface Forces : with Applications to Colloidal and Biological Systems* (Academic Press, San Diego, 1992).

[12] G. P. Crawford and S. Žumer, editors, *Liquid Crystals in Complex Geometries* (Taylor and Francis, London, 1996).

[13] J. M. Geary, J. W. Goodby, A. R. Kmetz and J. S. Patel, J. Appl. Phys. **62**, 4100 (1987).

[14] K. Weiss, C. Woll and D. Johannsmann, J. Chem. Phys. **113**, 11297 (2000).

[15] J. Cognard, *Alignment of Liquid Crystals and their Mixtures* (Gordon and Breach, London, 1982).

[16] D. Seo, J. Appl. Phys. **86**, 3594 (1999).

[17] D. Seo and S. Kobayashi, J. Appl. Phys. **86**, 4046 (1999).

[18] M. B. Feller, W. Chen and Y. R. Shen, Phys. Rev. A **43**, 6778 (1991).

[19] L. Xuan, T. Tohyama, T. Miyashita and T. Uchida, J. Appl. Phys. **96**, 1953 (2004).

[20] H. Yokoyama, S. Kobayashi and H. Kamei, J. Appl. Phys. **61**, 4501 (1986).

[21] S. Faetti, V. P. M. Gatti and T. J. Sluckin, Phys. Rev. Lett. **55**, 1681 (1985).

[22] M. Ibn-Elhaj and M. Schadt, Nature **410**, 796 (2001).

[23] S. Granick, S. K. Kumar, E. J. Amis, M. Antonietti, A. C. Balazs, A. K. Chakraborty, G. S. Grest, C. Hawker, P. Janmey, E. J. Kramer, R. Nuzzo, T. P. Russell and C. R. Safinya, J. Polym. Sci. B **41**, 2755 (2003).

[24] T. Gruhn and M. Schoen, J. Chem. Phys. **108**, 9124 (1998).

[25] P. Pasini and C. Zannoni, editors, *Advances in the Computer Simulations of Liquid Crystals* (Kluwer, Dordrecht, 2000).

[26] H. Steuer, S. Hess and M. Schoen, Phys. Rev. E **69**, 031708 (2004).

[27] D. Caprion and J. P. Ryckaert, J. Chem. Phys. **121**, 4874 (2004).

[28] D. L. Cheung and F. Schmid, J. Chem. Phys. **122**, 074902 (2005).

[29] L. Salamancha, A. Patrykiejew, Sokolowski and K. Binder, J. Chem. Phys. 074703 (2005).

[30] F. Barmes and D. Cleaver, Phys. Rev. E **69**, 061705 (2004).

[31] J. Quintana, E. C. Poire, H. Dominguez and J. Alejandre, Molec. Phys. **100**, 2597 (2002).

[32] C. Chiccoli, P. Pasini, S. Guzzetti and C. Zannoni, Molec. Cryst. Liq. Cryst. **360** (2001).

[33] N. Priezlev, G. Skačej, R. Pelcovits and S. Žumer, Phys. Rev. E **68**, 041709 (2003).

[34] G. Hongwei, F. Degang, L. Weng, X. Jie and X. Bing, Adv. Mater. **14**, 492 (2004).

[35] P. Cifra and T. Bleha, Macromolecules **34**, 605 (2001).

[36] A. Milchev, W. Paul and K. Binder, Macromol. Theory Simul. **3**, 305 (1994).

[37] M. Muller, J. Chem. Phys. **22**, 9930 (2002).

[38] V. Kuppa and E. Manias, J. Chem. Phys. **7**, 3421 (2003).

[39] H. P. Hsu and P. Grassberger, J. Chem. Phys. **4**, 2034 (2004).

[40] Y. Wang, J. Chem. Phys. **8**, 3898 (2004).

[41] O. B. Usta, A. J. C. Ladd and J. E. Butler, J. Chem. Phys. 094902 (2005).

[42] K. V. Workum and J. J. de Pablo, Nano Letters **3**, 1405 (2003).

[43] G. F. Hermsen, B. A. de Geteer, N. F. A. van der Vegt and M. Wessling, Macromolecules **35**, 5267 (2002).

[44] Y. Son, N. S. Martys, J. G. Hagedorn and K. B. Migler, Macromolecules **36**, 5825 (2003).

[45] J. J. Cerdá, T. Sintes and A. Chakrabarti, Macromolecules **38**, 1469 (2005).

[46] A. V. Berezkin, M. A. Solov'ev, P. G. Khalatur and A. R. Khokhlov, J. Chem. Phys. **121**, 6011 (2004).

[47] Q. Wang, Macromol. Theory Simul. **14**, 96 (2005).

[48] A. A. Collyer, Materials Science and Technology **5**, 309 (1989).

[49] R. Berardi, D. Micheletti, L. Muccioli, M. Ricci and C. Zannoni, J. Chem. Phys. **121**, 9123 (2004).

[50] J. G. Gay and B. J. Berne, J. Chem. Phys. **74**, 3316 (1981).

[51] C. Zannoni, J. Mater. Chem. **11**, 2637 (2001).

[52] R. Berardi, A. P. J. Emerson and C. Zannoni, J. Chem. Soc. Faraday Trans. **89**, 4069 (1993).

[53] R. B. Bird, R. C. Armstrong and D. Hassager, *Dynamics of Polymeric Liquids* (J. Wiley, New York, 1971).

[54] R. S. Khare, J. J. de Pablo and A. Yethiraj, Macromolecules **29**, 7910 (1996).

[55] D. Frenkel and B. Smit, *Understanding Molecular Simulations: From Algorithms to Applications* (Academic Press, San Diego, 1996).

[56] M. P. Allen and D. J. Tildesley, *Computer Simulation of Liquids* (Oxford University Press, Oxford, 1989).

[57] C. Zannoni, in *The Molecular Physics of Liquid Crystals*, edited by G. R. Luckhurst and G. W. Gray, chap. 3, 51–83 (Academic Press, London, 1979).

[58] U. Fabbri and C. Zannoni, Molec. Phys. **58**, 763 (1986).

[59] N. A. Clark, Phys. Rev. Lett. **55**, 292 (1985).

[60] Y. Ouchi, M. B. Feller, T. Moses and Y. R. Shen, Phys. Rev. Lett. **68**, 3040 (1992).

[61] P. J. Flory, *Principles of Polymer Chemistry* (Cornell University Press, Ithaca, 1953).

Boundary	RW	RP	UA	HOw	HOs
$f(\hat{\mathbf{u}}_i)$	1	1	$(\hat{\mathbf{u}}_i \cdot \hat{\mathbf{n}})^2$	1	1
α_i^A	1	1	1	1	1
α_i^B	1	1	1	0	0
K_w	9	9	9	18	36
cutoff	1	L_x	L_x	L_x	L_x

Table 1: Parameterizations of the particle–surface potential U_w^* (see Eq. 5 for description of the coefficients) for the anchoring conditions studied in this work: RW=repulsive wall, RP=random planar, UA=uniform alignment, HOw=weak homeotropic, and HOs=homeotropic strong.

Boundary	RP		UA		HOs		bulk	
T^*	2.8	3.8	2.8	3.8	2.8	3.8	2.8	3.8
C_{mon}	0.48	0.44	0.52	0.47	0.05	0.15	0.49	0.48
$\bar{x}_n$	52.9	48.0	56.4	51.8	5.7	16.8	53.1	51.5
$\bar{x}_w$	56.4	49.3	60.0	53.8	6.8	24.3	56.3	52.8
$\bar{I}_d$	1.1	1.0	1.1	1.0	1.2	1.5	1.1	1.0

Table 2: Standard average chain growth indeces: conversion C_{mon}, numeral $\bar{x}_n$ and weight $\bar{x}_w$ degrees of polymerization, and polydispersity index I_d obtained from the MC simulated polymerization for the different nano–confinements and temperatures described in the text.

T^*	Boundary	$\langle P_2^{(d)} \rangle$	$\langle {r_{ee}^*}^2 \rangle^{\frac{1}{2}}$	$\langle {r_{gyr}^*}^2 \rangle^{\frac{1}{2}}$	r_{max}^*	l_{ee}	$\frac{\langle {r_{ee}^*}^2 \rangle}{\langle {r_{gyr}^*}^2 \rangle}$
2.8	HOs	0.80	16.2	4.7	17.8	0.91	12.0
	UA	0.82	153.1	45.3	177.5	0.86	11.4
	RP	0.80	141.7	42.0	166.5	0.85	11.4
	bulk	0.82	147.0	43.2	167.1	0.88	11.6
3.8	HOs	0.23	17.7	6.6	52.8	0.34	7.2
	UA	0.29	60.7	22.6	163.0	0.37	7.2
	RP	0.04	33.2	13.5	151.1	0.22	6.0
	bulk	0.06	34.7	14.3	162.0	0.21	6.0

Table 3: Average second rank order parameter, end–to–end distance, and gyration radius and other indeces used to characterize chains length and shape of the bulk and confined samples as described in the text.

List of Figures

Figure 1: A sketch of the MC simulation cell setup, consisting of two confining planar surfaces perpendicular to the laboratory x axis. The periodic boundary conditions have been applied along y and z directions. We also show a monomer GB particle with two embedded surface interaction sites A and B, and a vector parallel to the surface $\hat{\mathbf{n}}$, and the angle β between the monomer axis and $\hat{\mathbf{n}}$.

Figure 2: Average order parameter $\langle P_2^{(d)} \rangle$ (plot (a)), and average energy per particle $\langle U^* \rangle$ (plot (b)) for the nano–confined GB monomers samples as function of the temperature T^*. The bulk energy profile in plot (b) has been taken from ref.[52]

Figure 3: Correlation function $g_w(x^*)$ at $T^* = 2.8$ (nematic phase, plot (a)) and $T^* = 3.8$ (isotropic phase, plot (b)) for nano–confined GB monomers samples: we also show from the left to the right the nematic and isotropic snapshots of the laboratory y axis views for the RP ($\langle P_2^{(d)} \rangle = 0.69$ (a), and 0.03 (b)), UA ($\langle P_2^{(d)} \rangle = 0.74$, and 0.27 (b)), and HOs ($\langle P_2^{(d)} \rangle = 0.71$, and 0.22 (b)) anchorings.

Figure 4: Three–dimensional views of the equilibrated confined polymeric samples for the RP plot (a), UA plot (b), and HOs plot (c) anchorings at temperature $T^* = 2.8$ (nematic phase, left column), and at $T^* = 3.8$ (isotropic phase, right column). The reference frame is also shown, while the monomeric particles and the confining surfaces have been omitted.

Figure 5: Correlation function $g_w(x^*)$ (left plot) and average order parameter $\langle P_2^{(z)}(x^*)\rangle$ (right plot) profiles for the equilibrated confined polymeric chains. Error bars have been plotted every 20 histogram points.

Figure 1

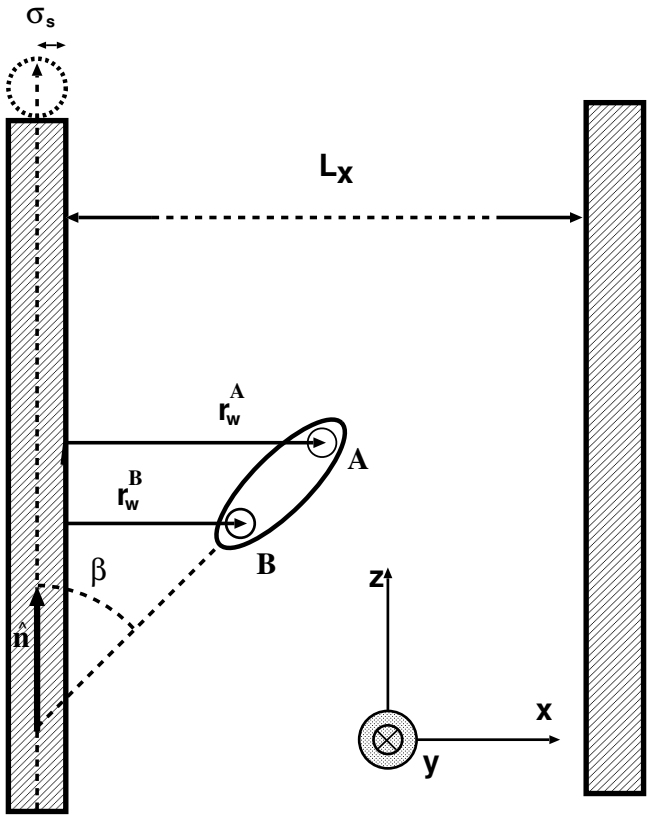

Figure 2

(a)

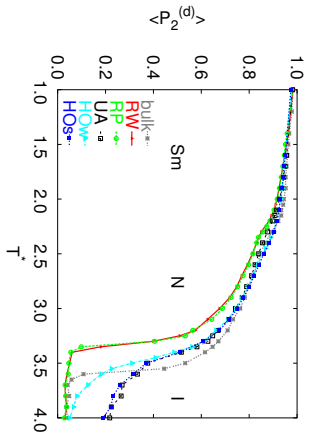

(b)

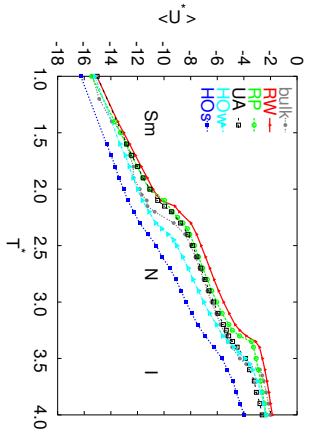

(a)

Figure 3

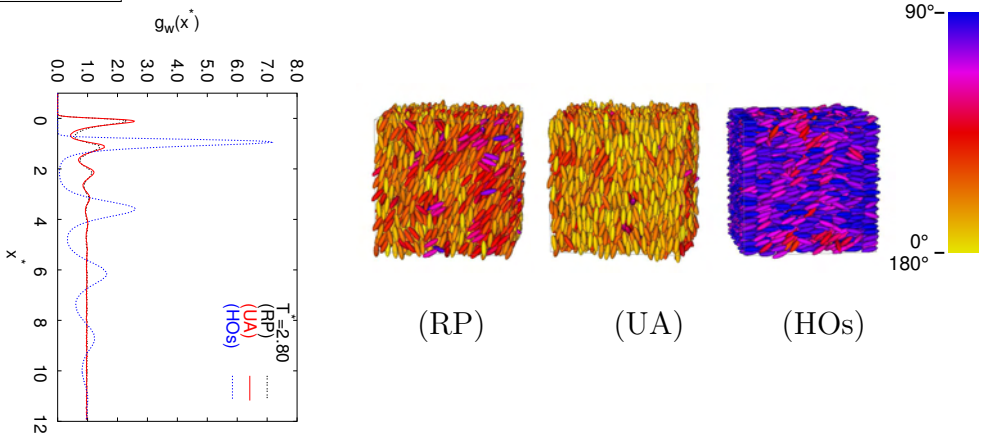
$g_w(x^*)$
x^*
T^*=2.80
(RP)
(UA)
(HOs)
90°
0°
180°
(RP)
(UA)
(HOs)

(b)

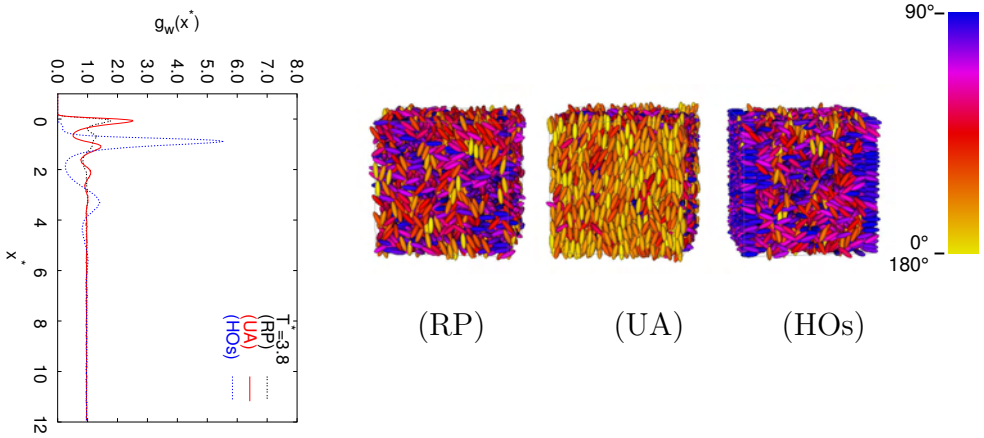
$g_w(x^*)$
x^*
T^*=3.8
(RP)
(UA)
(HOs)
90°
0°
180°
(RP)
(UA)
(HOs)

Figure 4

(a) RP

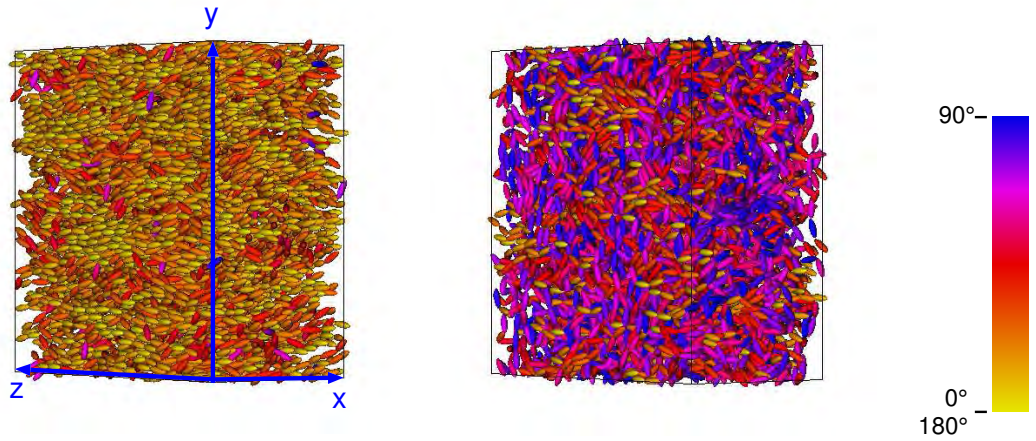

(b) UA

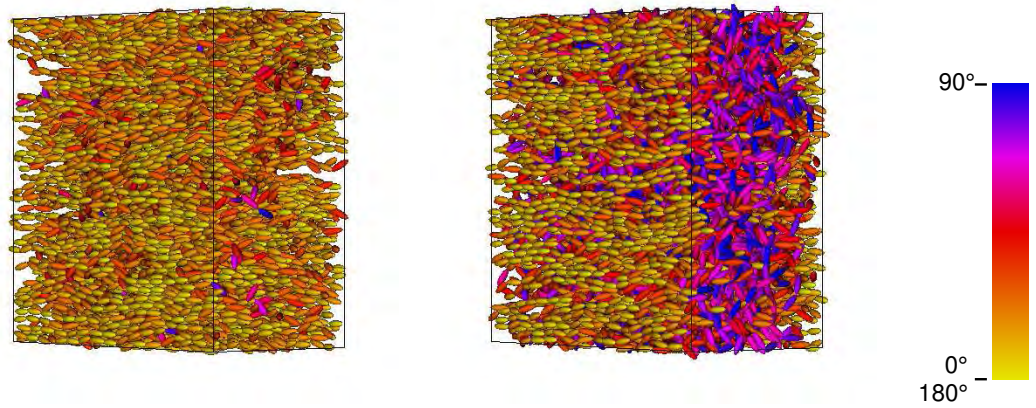

(c) HOs

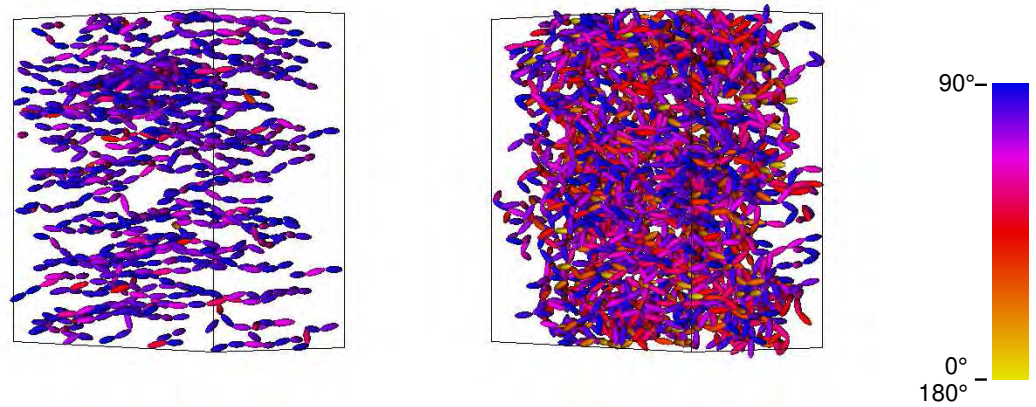

Figure 5

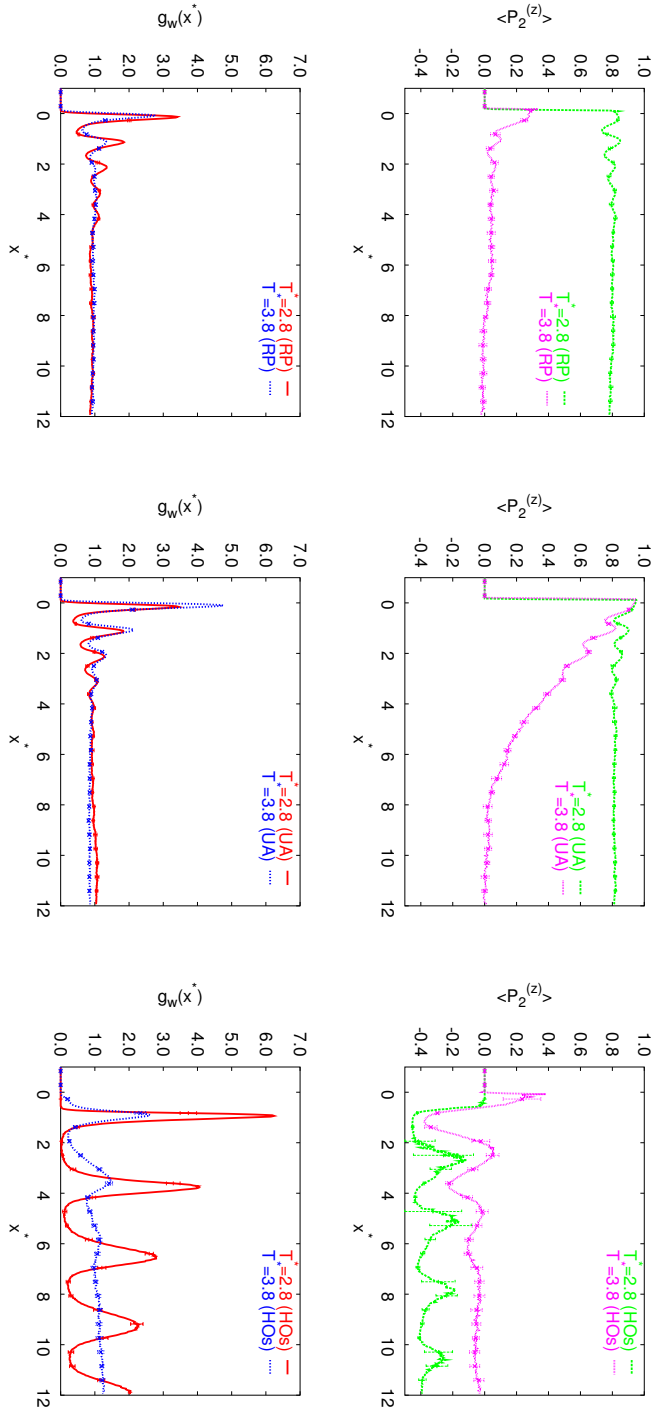
$\langle P_2^{(z)} \rangle$
$g_w(x^*)$
x^*
T^*=2.8 (RP)
T^*=3.8 (RP)
T^*=2.8 (UA)
T^*=3.8 (UA)
T^*=2.8 (HOs)
T^*=3.8 (HOs)